Hybrid Josephson junctions and their qubit applications

Vakhtel, T.

Chapter 1

Introduction

1.1 Preface

At the heart of this thesis is the Josephson effect – a condensed matter physics phenomenon of both fundamental and practical importance, one of the most exciting aspects of superconductivity. This effect occurs when a nanostructure, a weak link or an insulating barrier is placed between two superconductors. Such a device (Josephson junction) can sustain a dissipationless supercurrent that can flow without voltage bias. The effect is named after Brian Josephson, who provided its first mathematical description for the case of the tunneling barrier [1, 2]. The theoretical understanding and nanofabrication technique developments enabled numerous applications of such tunneling Josephson junctions; among the most famous ones are SQUID (superconducting quantum interference device) magnetometers, NIST standard of volt and superconducting qubits [3, 4]. The thesis focuses on the latter application, where further understanding of the Josephson effect in more complex devices may lead to improved properties of the qubits.

From the microscopic point of view, the ground states of the superconducting leads are condensates of Cooper pairs in a collective symmetry broken state, described by a complex order parameter. This complex order parameter has a phase, and, in a tunneling Josephson junction, the supercurrent will depend on the phase difference between the two superconductors ϕ in a non-linear way: $I \sim \sin\phi$. Due to the second Josephson relation $\dot{\phi} \sim V$, where V is the voltage drop across the junction, this non-linearity makes the junction a non-dissipative non-linear inductor. In

parallel with a capacitor and in the regime where ϕ is a quantum variable, such a system becomes a non-linear quantum oscillator, which happens to be one of the best pieces of hardware for a qubit. More sophisticated Josephson junctions may have more internal degrees of freedom and different current-phase characteristics [5]. These can be employed to design qubits even more robust to dephasing and decay.

The subject of Chapter 2 and Chapter 3 is a superconductor-quantum dot- superconductor (S-R-S) junction embedded in two different quantum circuits. In Chapter 2, we explore the circuit where the S-R-S junction is shunted (connected in parallel) with a capacitance. An essential characteristic of this system is the sensitivity of the spectrum to the fluctuations of the gate voltage used for the control of the qubit. We make detailed calculations of the dependence on the gate voltage while reproducing some previous theoretical predictions that, in some fine-tuned regime, the sensitivity should become extremely small.

In the second circuit, the capacitively shunted junction is additionally shunted with a linear inductor. In Chapter 3, we calculate energy splittings between states typically used for quantum computation. Such a system is one of the realisations of the so-called bi-fluxon qubit, where the coupling between $|0\rangle$ and $|1\rangle$ states is suppressed due to an additional conservation law forbidding the transition [6, 7].

Finally, Chapter 4 explores how the Josephson effect is modified in a junction containing a recently discovered class of magnetic materials: altermagnet. A distinct feature of such Josephson junctions is that the energy minimum may be achieved at the non-zero phase difference [8, 9], unlike in the tunneling junctions.

1.2 Josephson effects

We will start with the simplest type of a Josephson junction: superconductor-insulator-superconductor (S-I-S) junction. The second and third types are S-N-S (superconductor-semiconductor-superconductor) and S-R-S (superconductor-quantum dot-superconductor).

1.2.1 Tunneling Josephson junction

Tunneling (S-I-S) Josephson junction is the most widely used one for superconducting qubits. Usually, it's made of aluminium leads in the superconducting state with aluminium oxide in between; such a device can be

fabricated with the shadow evaporation technique. Each piece of the superconductors is described by a superconducting wave function $\psi = |\psi|e^{i\varphi}$: its amplitude corresponds to the superfluid density, and the phase is referred to as the superconducting phase. Because there is a small but non-zero overlap between the two wavefunctions, a Cooper pair can tunnel, and a non-zero supercurrent will flow. The low energy Hamiltonian of such a junction is :

$$H(\phi) = -E_J \cos\phi, \tag{1.1}$$

E_J is the positive Josephson energy, and ϕ is the superconducting phase difference between the two leads. Because the charge (in the units of the Cooper pair charge) operator is canonically conjugated to phase, the charge operator is:

$$\hat{n} = -i\partial_\phi. \tag{1.2}$$

Then, the current-phase relation is given by:

$$I(\phi) = 2eE_J \sin\phi. \tag{1.3}$$

This is the well-known first Josephson relation. A version of the celebrated Ambegaokar-Baratoff formula connects E_J to the normal state conductance G_N of the junction [10–12]:

$$E_J = \frac{G_N}{G_Q}\frac{\Delta}{8}, \quad G_Q = \frac{e^2}{h}, \tag{1.4}$$

where Δ is the superconducting gap. If there is a non-zero voltage drop V across the junction, the Josephson relation says $\dot{\phi} = 2eV$. This relation can be derived from gauge invariance reasonings and relates the superconducting phase to the flux. It allows to compute the inductance of the junction $L_J^{-1} = \frac{\partial^2 E(\phi)}{\partial\phi^2}$. The non-linear inductance is one of the properties that make Josephson junctions an important element of superconducting qubits, as will be discussed further.

1.2.2 Andreev reflection

In the tunneling junction, the Josephson energy and the supercurrent can be derived using second-order perturbation theory [13]. In an S-N-S junction, the coupling between the leads generally cannot be treated as

a perturbation. Therefore, a more microscopic approach to the origin of the supercurrent is needed. Let us consider a perfect NS (normal metal-superconductor) interface first. Suppose, from the normal side, there is an incident electron with energy $E < \Delta$ (measured from the Fermi energy), meaning it cannot enter the superconductor. Naively, no charge transfer can happen in this situation. Nevertheless, superconductivity allows charge transfer via Andreev reflection when the electron gets reflected as a hole [14]. Because the total charge has to be conserved, an additional Cooper pair was created in the superconductor, so the transferred charge is $2e$. Since the excitation energy inside the normal part has to stay the same: $E = v_F(k_e - k_F) = -v_F(k_h - k_F)$ and $k_e - k_h = 2E/v_F$. Usually, the coherence length $\xi \equiv v_F/\Delta \gg 1/k_F$, so the momenta are almost the same (Andreev approximation). However, the hole's velocity will be the opposite of the electron's, hence the name reflection. A reverse process, when a hole is reflected as an electron, can also happen. One can match the electron/hole wavefunction to the solution of the Bogoliubov-de Gennes equation in the superconducting part and obtain that the reflected hole/electron also acquires a relative phase [13]:

$$\chi = -\arccos\left(\frac{E}{\Delta}\right) \mp \varphi, \tag{1.5}$$

where $-/+$ is for the incident electron/hole case.

1.2.3 S-N-S junction

A closed trajectory becomes possible if one has an SNS junction instead of one NS interface. First, an electron is Andreev reflected as a hole, and then the hole propagates to the other SN interface and is reflected again as an electron. Such a bound motion implies the possibility of a state localized in the junction called the Andreev bound state. Note that a Cooper pair is transferred between the leads after these two processes so that such states may carry a supercurrent. Often, one assumes a short junction limit $L \ll \xi$, in which the accumulation of phase due to ballistic propagation of an electron/hole $(k_e - k_h)L$ can be neglected. In this case, the Andreev bound states' energies obtained from the scattering formalism are [15]:

$$E_{\mathrm{ABS}}(\phi) = \Delta\sqrt{1 - T\sin^2(\phi/2)}, \tag{1.6}$$

where T is the transmission eigenvalue of the junction. These states are spin-degenerate and are the only ones that contribute to the supercurrent in the short-junction limit, as the continuum contribution is negligible. Usually, there are multiple Andreev bound states that originate from multiple channels at the Fermi energy. The tunneling Josephson potential 1.1 can be obtained from 1.6 by the Tailor expansion around $T_n = 0$, where n stands for each channel contributing to the in-gap spectrum. The correspondence reads $E_J = \Delta \sum_n T_n/4$. Note that formally, because the tunneling junctions are usually only 1 atom thick, the scattering matrix approach for the Andreev bound states' spectrum does not apply, as one cannot insert leads inside the normal part of the junction. Nevertheless, the formula works.

1.2.4 S-R-S junction

The previous model, however, doesn't describe all the typical experimental situations. Some of the InAs-Al-shell Josephson junctions rather look like a small confined region (quantum dot) weakly coupled to the leads (with the tunneling rates Γ_1, Γ_2) [16, 17]. We assume that this region hosts a single spin-degenerate level. If the dwell time $\tau_{dw} = \Gamma^{-1} \equiv 1/(\Gamma_1 + \Gamma_2) \gg \Delta^{-1}$, then this junction is in the opposite to the short junction $\tau_{dw} = L/v_F \ll 1/\Delta$ limit, and it will have different properties. In what follows, we will focus exactly on the tunneling $\tau_{dw} \gg \Delta^{-1}$ limit. In a more general case, the Andreev bound states' energies cannot be written in a closed form [5]. We will also assume that the total number of the electrons in the leads and on the dot is even, such that at 0 temperature, it's sufficient to consider only two possible occupation numbers of the quantum dot (0 and 2). Given these assumptions, the low-energy Hamiltonian is [18–21]:

$$H_{QD} = 4E_C(-i\partial_\phi - n_g)^2 + V(\phi) \tag{1.7}$$

$$V(\phi) = -\epsilon_r \tau_z - \Gamma \cos(\phi/2)\tau_x - \delta\Gamma \sin(\phi/2)\tau_y, \tag{1.8}$$

where the Pauli matrices act in the occupation number of the dot space, $\delta\Gamma = \Gamma_1 - \Gamma_2$ and ϵ_r is the detuning of the resonant level from the Fermi energy in the leads. There's also a capacitive energy with $E_C = e^2/2C$ (where C is the capacitance of the junction) due to the dipole moment generated by Cooper pair tunneling and equilibrium charge n_g controlled by a gate (in the Cooper pair charge units), shown on the circuit. Note that the Hamiltonian is not 2π-periodic. This is because it is written in a

2π-anti-periodic basis, with twisted boundary conditions [22]:

$$\Psi(\phi + 2\pi) = \tau_z \Psi(\phi). \tag{1.9}$$

The Fourier decomposition of these basis states in terms of the states with well-defined charge is:

$$\begin{aligned} \Psi_0(\phi) &= \sum_{n\in\mathbb{Z}} e^{i\phi n}\Psi_0(n), \\ \Psi_2(\phi) &= \sum_{n\in\mathbb{Z}+\frac{1}{2}} e^{i\phi n}\Psi_2(n). \end{aligned} \tag{1.10}$$

Here, n is the charge transferred across the junction, as this is the variable related to the dipole moment. In the second sum, the summation goes over half-integer n because when the quantum dot is occupied twice, it amounts to $1/2$ of the Cooper pair transfer. Hence, the Hamiltonian is $2\pi-$periodic if one accounts for the aperiodicity of the basis. The eigenvalues of $V(\phi)$ are $\pm E_A(\phi)$, where E_A happens to be the same as the Andreev bound state's energy (due to spin degeneracy):

$$E_A = \Gamma_A\sqrt{1 - T\sin^2\phi/2}, \quad \Gamma_A = \sqrt{\Gamma^2 + \epsilon_r^2}. \tag{1.11}$$

$T = 1 - |r|^2$ is the effective transparency of the junction with $r = \frac{\epsilon_r + i\delta\Gamma}{\Gamma_A}$. The spectrum is similar to that of SNS, but the Andreev bound states are detached from the continuum, and the wavefunctions are different. The effects of this difference on the qubit are discussed in Chapters 3 and 2. Usually, a quantum dot has a non-negligible (Anderson U) Coulomb energy. This can make an odd-occupied Andreev bound state the ground state of the junction [23], especially if the transparency is almost perfect. However, this energy can be neglected if $\Gamma \gg U$ [18] and the quantum dot cannot be occupied only once at zero temperature if the total number of electrons in the circuit is even.

1.3 Superconducting qubits

Superconductors offer a promising platform for quantum computation because: a) A single piece of a superconductor has a non-degenerate ground state and b) the excitations of this ground state are separated by a superconducting gap. If the qubit's energies are deep within the gap, the

coupling to the continuum degrees of freedom is suppressed. Usually, the superconducting gaps are of the order of ~ 100 GHz, and the qubits are operated at the $1-10$ GHz energies, so the system has to be cooled down to ~ 10 mK. The most naive qubit would be a quantum version of a harmonic oscillator: an inductor in parallel with a capacitor. However, this system has an obvious problem: one cannot address a specific transition because the levels are equidistant. In the previous section 1.2.1, we learned that a Josephson junction is a non-linear inductor, which makes it a useful part of a qubit. The following two subsections briefly discuss two common types of qubits based on tunneling Josephson junctions.

1.3.1 Transmon qubit

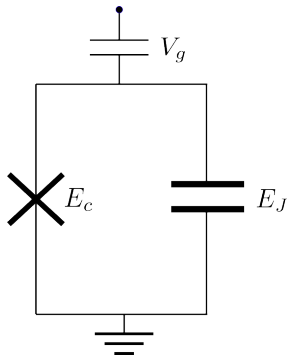

Figure 1.1. Transmon circuit

If a Josephson junction is shunted by a capacitor, similarly as in 1.2.4, the Hamiltonian of such a circuit is [24, 25]:

$$\hat{H} = 4E_C \left(\hat{n} - n_g\right)^2 - E_J \cos\hat{\phi}. \tag{1.12}$$

The number of Cooper pairs on the island is an integer, so the boundary conditions are periodic $\psi(\phi+2\pi) = \psi(\phi)$ as $e^{in(\phi+2\pi)} = e^{in\phi}$ if $n \in \mathbb{Z}$. The eigenvalue problem is mathematically equivalent to that of an electron in the periodic crystal. ψ satisfies the same differential equation as a Bloch wave with quasi-momentum n_g. One can always make a gauge transformation $\psi \to \psi e^{-i\phi}$, which preserves the periodic boundary conditions but changes n_g by 1. Hence, the spectrum will be periodic in n_g. We consider two illustrative limits.

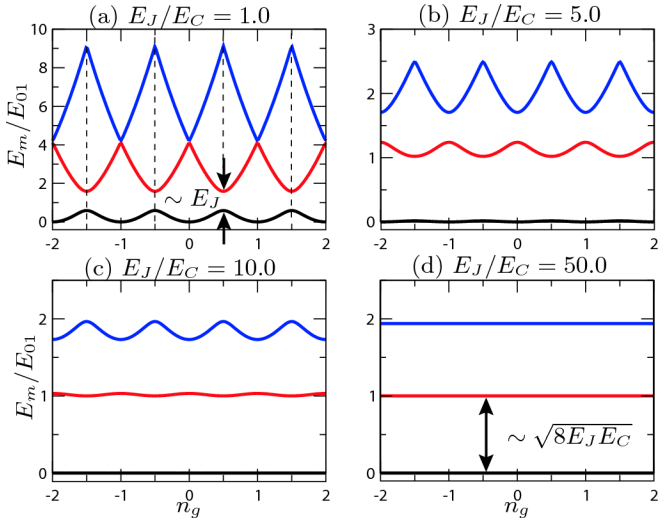

Figure 1.2. Eigenenergies of the transmon Hamiltonian 1.12 as a function of n_g for different ratios E_J/E_C. Energies are given in units of the transition energy E_{01} between the ground and first excited state, evaluated at $n_g = 1/2$. *Reprinted figure with permission from J. Koch, Terri M. Yu, J. Gambetta, A. A. Houck, D. I. Schuster, J. Majer, A. Blais, M. H. Devoret, S. M. Girvin, and R. J. Schoelkopf, Phys. Rev. A* ***76****, 042319, 2007. Copyright (2007) by the American Physical Society*

Cooper pair box $E_C \gg E_J$ regime

One will typically end up in this situation if the junction is not shunted by a big capacitor on purpose. The spectrum of the junction is then very similar to that of a nearly free electron, where the Cooper pair tunneling introduces the avoided crossings between the charge parabolas. Such a qubit has a high degree of anharmonicity [26], but its energy depends strongly on n_g. A gate that controls this equilibrium charge typically fluctuates, leading to the dephasing of the qubit. That is why this regime is suboptimal, and the next regime we will consider is much better.

Transmon $E_C \ll E_J$ regime

A large capacitor $\sim 100\ \mu m$ size allows to achieve it. Low-lying levels are localized in the minima of the potential, and the tunneling between these minima, also called phase slips, is exponentially suppressed. The

tight-binding spectrum for the m-th band is:

$$E_m(n_g) = \omega_p(m + 1/2) - \frac{\epsilon_m}{2}\cos(2\pi n_g). \tag{1.13}$$

ϵ_m is given by a WKB formula, which is true also for the lowest levels, where the usual WKB does not work [26]:

$$\boldsymbol{\epsilon}_m \simeq (-1)^m \frac{2^{4m+5}}{m!}\sqrt{\frac{2}{\pi}}\left(\frac{E_J}{2E_C}\right)^{\frac{m}{2}+\frac{3}{4}} e^{-\sqrt{8E_J/E_C}}. \tag{1.14}$$

$\omega_p = \sqrt{8E_JE_C}$ is called plasma frequency, which corresponds to the harmonic oscillations in the quadratic part of the Josephson potential. The sensitivity of the spectrum to n_g (also called charge dispersion) is exponentially small, but the energy levels are almost harmonic again. Nevertheless, an algebraically small anharmonicity $\sim \sqrt{E_C/E_J}$ that remains is sufficient. To illustrate the limits mentioned above, the spectra at various E_J/E_C ratios are plotted in the Figure **??**.

1.3.2 Fluxonium qubit

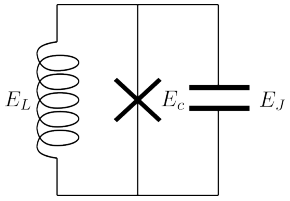

Figure 1.3. Fluxonium circuit

Another way to eliminate the charge dispersion while maintaining a much larger level of anharmonicity is to implement it in another type of superconducting qubit called fluxonium [27, 28]. The idea is to get rid of the superconducting island by shunting it with an inductor:

$$\hat{H} = 4E_C(\hat{n} - n_g)^2 + \frac{1}{2}E_L\left(\hat{\phi} + \phi_{ext}\right)^2 - E_J\cos\phi. \tag{1.15}$$

E_L is related to the inductance as $E_L = \left(\Phi_0/2\pi\right)^2/L$ and ϕ_{ext} is related to the flux threaded through the loop $\phi_{ext} = \Phi/\Phi_0$, where $\Phi_0 = h/2e$ is the flux quantum. The charge on the island is not quantized anymore, so any induced charge n_g in the kinetic term can be gauged away, and

the spectrum is insensitive to it. Phase slips can also happen in the inductor, introducing infinitely many copies of the inductive term shifted by 2π. However, if the phase slips happen at time scales much larger than the time scale of the experiment, it's sufficient to keep only one. Despite the simplicity of the Hamiltonian, its physics is very rich. We focus on the regime where $E_L \ll \omega_p$ & $E_C \ll E_J$. For the analysis, it is convenient to write the Hamiltonian in the basis of the Bloch waves $\Psi_{p,s}(\phi) \equiv \langle \phi | s, p \rangle = e^{-ip\phi} u_{p,s}(\phi)$. $u_{p,s}(\phi + 2\pi) = u_{p,s}(\phi)$ is periodic and diagonalizes the 'transmon' part:

$$\left(4E_C(\hat{n} - p)^2 - E_J \cos\phi\right) u_{p,s} = E_s(p) u_{p,s}. \tag{1.16}$$

$p \in (0, 1]$ denotes the 'quasi-momentum' and s denotes the band index. $\Psi_{p,s}(\phi)$ are the functions of the non-compact phase and form a complete orthonormal basis if $u_{p,s}$ are normalized to 1 on the circle $\phi \in (0, 2\pi]$. The phase $\hat{\phi}$ in the basis is expressed as follows:

$$\hat{\phi} = -i\partial_p + \hat{\Omega}. \tag{1.17}$$

The matrix elements of this operator [27, 29]

$$\langle p, s | \hat{\Omega} | p', s' \rangle = \delta(p - p') \Omega_{s,s'}(p) \tag{1.18}$$

$$\Omega_{s,s'}(p) = -\left(\frac{2E_C}{E_J}\right)^{1/4} \left(\sqrt{s}\delta_{s+1,s'} + \sqrt{s+1}\delta_{s',s-1}\right) \tag{1.19}$$

can be neglected in our limit, such that the Hamiltonian has a block-diagonal structure:

$$H_s = \frac{E_L}{2}(-i\partial_p + \phi_{ext})^2 + E_s(p). \tag{1.20}$$

The wavefunctions in this basis are also periodic $\psi_s(p + 1) = \psi_s(p)$. Because $E_s(p) = E_s(1/4) - \frac{\epsilon_s}{2} \cos 2\pi p$ (1.13), this Hamiltonian is dual (under the exchange of the quasi-charge and the phase) to transmon. Hence, we discuss the two regimes again.

Usual fluxonium $E_L \gg \epsilon_s$ regime

The reason for the title is that it is the most common fluxonium regime, which is the easiest to achieve experimentally. Like in the $E_C \gg E_J$ regime

of transmon, E_s is a perturbation on the top of the kinetic $\frac{E_L}{2}(-i\partial_p+\phi_{ext})^2$ term, whose eigenstates are fluxons:

$$|2\pi m, s\rangle = \int_0^1 dp e^{i2\pi mp}|p, s\rangle, \quad m \in \mathbb{Z}. \tag{1.21}$$

This is again a complete basis of states [27, 29]. In the phase representation, the fluxons $\langle\phi|2\pi m, s\rangle$ are states localized around $\phi = 2\pi m$ minima of the Josephson energy, originating from the $s-$th harmonic levels. $E_s(p)$ acts like a weak scattering potential, coupling neighbouring fluxons and introducing the avoided crossings. Similarly to the Cooper pair box, the levels are highly anharmonic, but the spectrum depends strongly on the flux bias ϕ_{ext}. One can operate the qubit at $\phi_{ext} = \pi$, where one of the avoided crossings for the lowest band happens, and the first derivative of the energy difference with flux vanishes. This is a so-called sweet spot where most of the modern fluxoniums are operated. In the phase ϕ space, the $|0\rangle, |1\rangle$ wavefunctions are the symmetric and antisymmetric superpositions of fluxons localized at $\phi = -2\pi$ and $\phi = 0$. Extremely large coherence times were achieved with this type of qubit, of the order of 1ms [30–33].

Blochnium $E_L \ll \epsilon_s$ regime

This regime is tough to achieve, as it requires very small inductances due to the exponential suppression of the phase slips. Thus, this regime has been reached experimentally only marginally [34]. The lowest states are localized in the quasi-charge minima of $E_0(p)$ and are dual to those in the transmon $E_J \gg E_C$ regime. Hence, in this regime, the qubit's energies are insensitive to both n_g and ϕ_{ext} fluctuations, which is why achieving it would be highly desirable.

1.4 Minimally twisted bilayer graphene

It was predicted more than 10 years ago that stacking two graphene layers at the top of each other at a small angle ($\theta \sim 1^\circ$) leads to the appearance of flat bands [35, 36]. Flat bands enable a variety of strongly correlated phenomena and remarkable tunability of the material [37–39], the study of which led to the emergence of a new field: twistronics [40]. However, also at small angles $\sim 0.1^\circ$, where interactions can be neglected in certain cases,

interesting physics can happen [41–43]. The magnetotransport properties of such a material, called minimally twisted bilayer graphene, are discussed in Chapter 5 and Chapter 6.

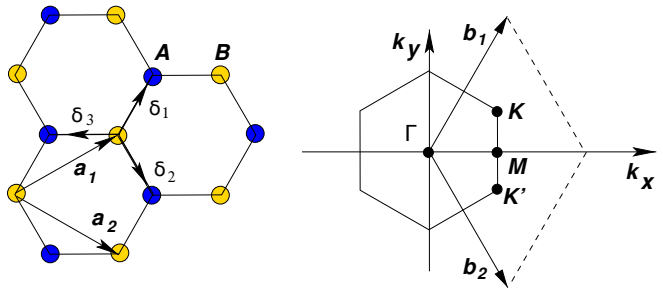

Figure 1.4. Graphene honeycomb lattice and its Brillouin zone. *Reprinted figure with permission from A. H. Castro Neto, F. Guinea, N. M. R. Peres, K. S. Novoselov, and A. K. Geim, Rev. Mod. Phys.* ***81****, 109, 2009. Copyright (2009) by the American Physical Society.*

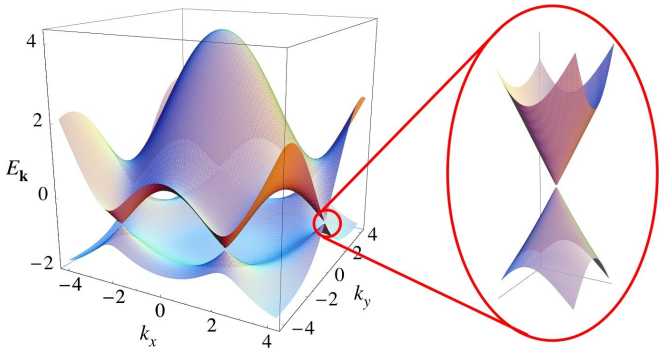

Figure 1.5. Graphene band-structure. *Reprinted figure with permission from A. H. Castro Neto, F. Guinea, N. M. R. Peres, K. S. Novoselov, and A. K. Geim, Rev. Mod. Phys.* ***81****, 109, 2009. Copyright (2009) by the American Physical Society.*

First, we recall the basic properties of single-layer graphene. The material is made of carbon atoms arranged in a hexagonal 2D lattice (lattice constant 2.46 Å) [44]. The unit cell has two atoms 1.4, which are usually named A and B. Figure 1.6 shows the band structure in the simplest tight-binding model. There are two special points (K and K') in the Brillouin zone where the two Dirac cones are (Fig. 1.5), with linear dispersion

relations $E = \pm v_F|k|$ in their neighbourhoods. The value of v_F is of the order of 10^6 m/s. The valley (K or K') index becomes an almost good quantum number at low enough energies and in the absence of short-scale disorder.

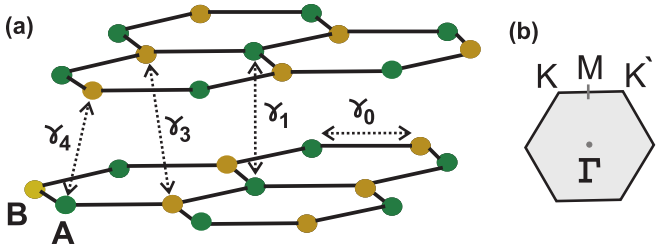

Figure 1.6. Lattice structure of Bernal AB stacking configuration of bilayer graphene and the corresponding Brillouin zone. *Reprinted figure with permission from A. H. Castro Neto, F. Guinea, N. M. R. Peres, K. S. Novoselov, and A. K. Geim, Rev. Mod. Phys.* ***81****, 109, 2009. Copyright (2009) by the American Physical Society.*

Second, we introduce Bernal stacked bilayer graphene, which is the lowest energy stacking configuration. In an AB (BA) configuration, the B(A) atoms will be on the top of the centres of the hexagons in the bottom layers (Fig. 1.6) . The effect on the band structure is that the Dirac cones from the two layers hybridize and become parabolas, as shown in the Figure 1.7. Two of these parabolas touch at each Dirac point. If a perpendicular electric field is applied (by gating the material), a gap proportional to the strength of the field opens. As a result, the material becomes a semiconductor with a tunable gap. Another important feature is that each valley has a non-trivial Chern number ± 1, even though the total Chern number is 0 [44].

Finally, when the two layers are stacked at a very small $\sim 0.1^\circ$ angle, a superlattice with a large $\sim$ 100 nm unit cell appears [45–47]. Such twist angles can even happen in nature [48]. Because Bernal stacking is the lowest energy configuration [44], the lattice will relax into sharply defined triangular AB/BA domains, as shown in the Figure 1.8. As already explained, the domains become gapped if a perpendicular electric field is applied. Gapped AB and BA domains will have the opposite (± 1) Chern numbers for a fixed valley index. As a result, a topological phase transition happens across each domain wall, and because the Chern number changes by 2, there will be two chiral modes around each domain for one valley and

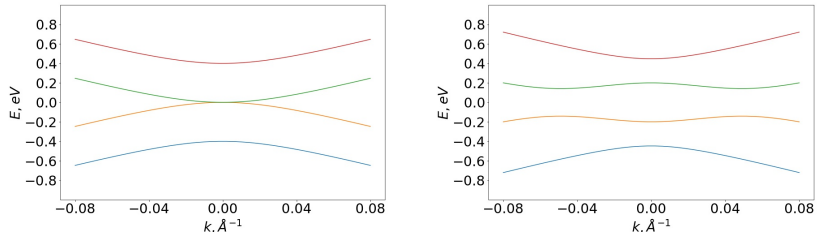

Figure 1.7. *Left panel*: Band-structure of Bernal stacked bilayer graphene *Right panel*: Band-structure of Bernal stacked graphene with perpendicular electric field applied.

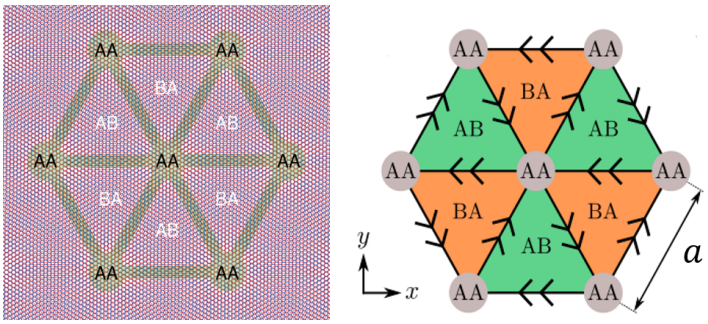

Figure 1.8. *Left panel*: Moire pattern of minimally twisted bilayer graphene *Reprinted figure with permission from J. D. Verbakel, Q. Yao, K. Sotthewes, and H. J. W. Zandvliet, Phys. Rev. B* ***103****, 165134, 2021. Copyright (2021) by the American Physical Society. Right panel*: Network model for transport in electrically gated minimally twisted bilayer graphene. *Reprinted figure with permission from C. De Beule, F. Dominguez, and P. Recher Phys. Rev. Lett.* ***125****, 096402, 2020. Copyright (2020) by the American Physical Society.*

spin. The network of these states was experimentally observed with STM [48, 49], and the absence of inter-valley scattering due to disorder, which is crucial for the arguments, was confirmed as well [48]. The direction of propagation of the modes is reversed for the opposite valley, which ensures the T-reversal symmetry. Typically, it's assumed that the modes propagate ballistically along the boundaries of the domains and scatter according to some scattering matrix in the nodes with AA alignment of the atoms [41, 43]. This model was successful in describing magnetotransport experiments [50, 51].

1.5 Bloch oscillations

An important concept that will be encountered in Chapter 5 and Chapter 6 is Bloch oscillations. This is one of the counterintuitive phenomena in crystals: if a weak electric field is applied, the velocity of the electrons will oscillate with frequency eEa (where E is the strength of the electric field and e is the charge of the electron) due to the Bragg reflection [52, 53]. Despite early predictions, it has not been measured in a crystal, as for the typical electric fields and lattice constants, the mean free times of the electrons are typically too low. However, it's been observed in superlattices [54–58] and a mathematical analogue of Bloch oscillations in minimally twisted bilayer graphene, which should be possible to observe, will be discussed in the Chapter 5.

The simplest model where Bloch oscillations can be explained is a 1D tight-binding model of non-interacting electrons in a lattice. The dispersion relation will be $E = h \cos ka$, where a is the lattice constant, k is the quasi-momentum and h is the hopping strength. If a sufficiently weak electric field is applied to the crystal, such that the single-band model stays intact, this will generate a force on the electrons $\dot{k} = -eE$. The equation is trivial to integrate: $k(t) = k_0 - eEt$. This means that the velocity $v(k) = \partial_k E$ of each electron will oscillate in time due to the periodicity in k dispersion relation, and an AC current will be generated.

If we imagine a semi-classical wave-packet, localized around $z(0)$ at the lengthscale $\gg a$ with some quasi-momentum $= q$, its position will oscillate in time too:

$$z(t) - z(0) = \int_0^t \partial_k \epsilon(k) dt' = \frac{h}{eE}(\cos(k_0 a - eEta) - \cos(k_0 a)). \quad (1.22)$$

However, if the wave packet is localized only at the scale of one lattice constant, and the quasimomentum is not well-defined, the probability density will have the oscillation pattern of the so-called breathing mode [59], shown in the Figure 1.9. The horizontal axis corresponds to time and the vertical axis corresponds to the position (z). The wave packet returns to the initial lattice site exactly after one period of oscillations: $T = \frac{2\pi}{eEa}$, unlike in the semi-classical case, where such return happens twice during the period.

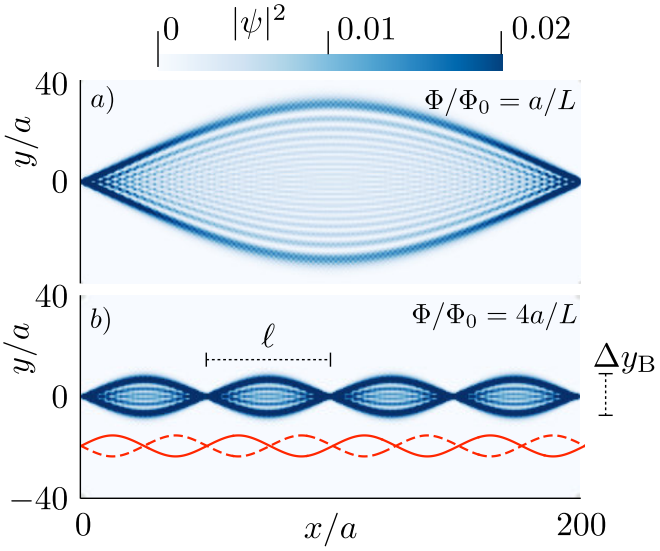

Figure 1.9. Breathing mode for a state initially localized at the origin. The colour scale stands for the probability density of the wave packet. The image below illustrates that the semi-classical wavepacket returns to the origin twice during one Bloch period of oscillation, while the breathing mode does so only once

1.6 Altermagnets

There are two well-known magnetic phases that have collinear spins and are enabled by exchange interactions: ferromagnetism and antiferromagnetism. However, in the recent 5 years, a new, third phase was theoretically predicted: altermagnetism [60–63]. It shares some similarities with both phases. Like in ferromagnets, the time-reversal symmetry is broken, which leads to the anomalous Hall effect [63–66], confirmed experimentally in semiconducting MnTe [67] and metallic RuO_2 [68]. Like antiferromagnets, altermagnets have no net magnetization [64, 65, 69, 70]. However, there are also cases where altermagnets behave like neither of the two, one of them will be considered in this thesis.

The simplest Neel antiferromagnet can be seen as follows. Let's imagine a 1D crystal lattice of magnetic ions having collinear spins. Every second spin is flipped with respect to the neighbouring spin, and one can divide the chain into two opposite spin sub-lattices, which are related by a translation by one unit cell. Since the Hamiltonian should be sym-

metric under such a translation, for both spins the electronic dispersion relation will be the same and the Hamiltonian will be time-reversal symmetric, hence the 0 net polarization. Also more sophisticated versions of antiferromagnets exist, where two spin sub-lattices can be connected by inversion. However, the magnetic properties of such materials are the same as those of the Neel antiferromagnets at the qualitative level [69].

Another possibility can theoretically happen; when two sub-lattices are related by neither inversion nor translation. For example, it can be a rotation, like in RuO_2 [64, 71]. Because the atoms with opposite spins are rotated by $\pi/2$ relative to each other, the dispersion relations for the two spins are no longer the same, but related by the same rotation. A

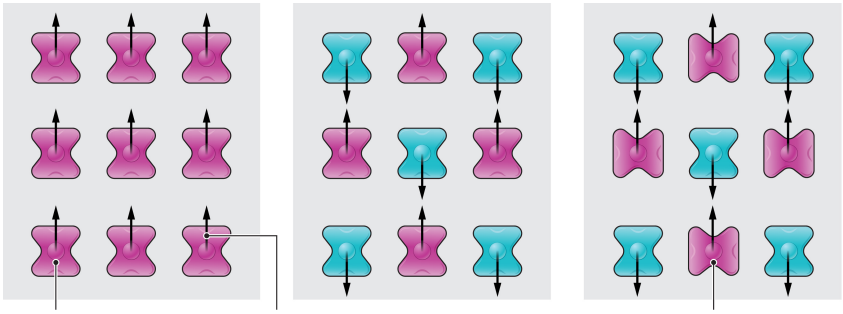

Figure 1.10. Example configurations of spins and atoms for three magnetic phases: ferromagnetism, antiferromagnetism and altermagnetism. In altermagnetic RuO_2, atoms with opposite spins are rotated by $\pi/2$. *From Savitsky, Zack. "Researchers discover new kind of magnetism." Science (New York, NY) 383.6683 (2024): 574-575. Reprinted with permission from AAAS.*

minimal model for such a material is the following [72] (Fig. 1.11):

$$H = \frac{1}{2m}\left(k_x^2 + k_y^2\right)\sigma_0 - t(k_x^2 - k_y^2)\sigma_z, \tag{1.23}$$

where k_x, k_y are the momenta and σ_z is the Pauli matrix acting in the spin space. The first term corresponds to the usual isotropic contribution and the second term is the altermagnetic one. This term is also referred to as d-wave magnetism – a magnetic counterpart to the d-wave superconducting order parameter (in that sense, s-wave magnetism is a ferromagnet) [65]. It's immediately obvious that the time-reversal symmetry is broken, and the Fermi-surface is spin-split. These two important signatures have been recently verified experimentally [71, 73]. Nevertheless, the net

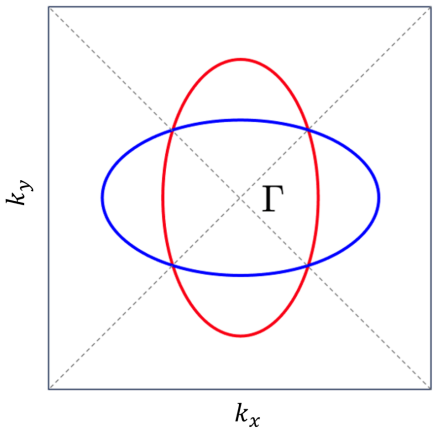

Figure 1.11. Fermi surface of an altermagnetic material. Blue colour stands for the spin up and red colour stands for the spin down. *By Libor Šmejkal - Provided by the author, CC BY-SA 4.0.*

magnetization is 0, since the two Fermi-surfaces are the same up to the rotation. Note, that unlike spin-orbit coupling, which doesn't break time-reversal symmetry, this interaction is quadratic in momentum and is of non-relativistic origin (it can be caused by exchange interactions, as mentioned in the beginning). Due to the latter fact, t is predicted to be quite large in some materials, up to ~ 1 eV [65, 72, 74].

Despite the recent discovery, this phenomenon is believed to be quite common; there are dozens of such materials already [65], some of them (such as MnTe) were initially believed to be antiferromagnets [75]. One of the experimental obstacles is the existence of domains, which makes many of the predicted effects cancel [76]. Despite the difficulty, this novel magnetic phase is worth studying from both fundamental and practical points of view, as the unique combination of spin-polarized Fermi surface and the absence of net magnetization makes it a promising material for spintronics [65].

A relatively recent direction of research is the study of the interplay between superconductivity and altermagnetism. A number of interesting phenomena have been already discovered: orientation-dependent Andreev reflection [77, 78], π Josephson junction [8, 9] and topological Majorana modes [79, 80]. In Chapter 4 we study the second effect in a more microscopic and non-perturbative way by calculating the Andreev Bound states'

spectrum for arbitrary transparency. We recover the π junction behaviour and observe a large anisotropy with respect to the orientation of the altermagnet in the normal part. This provides us with an example when altermagnet behaves neither as a ferromagnet, nor an antiferromagnet: an antiferromagnetic junction wouldn't show the π junction behaviour, but a ferromagnetic junction doesn't have such large anisotropy.

1.7 This thesis

Bellow I briefly highlight the main results presented in the thesis.

1.7.1 Chapter 2

In the second chapter, we compute analytically the amplitudes of 2π and 4π phase slips occurring in a resonant level capacitively shunted Josephson junction, which determines the charge dispersion of the transmon qubit. The amplitude for quantum tunneling under the Josephson potential barrier is modified by the Landau-Zener amplitude of adiabatic passage through an Andreev level crossing, resulting in the suppression of 2π phase slips. The Landau-Zener amplitude vanishes when the level is on resonance with the Fermi energy in the leads and the couplings are symmetric (which corresponds to high effective transparency of the junction). As a consequence, 4π phase slips become the dominant tunneling process. The analytical expressions demonstrate this crossover, showing that a very small residual charge dispersion persists even at perfect transparency. These results are of relevance to the experimental observation of the vanishing charge dispersion in the InAs-Al shell nanowire transmons [16, 17].

1.7.2 Chapter 3

The next chapter considers a fluxonium circuit consisting of a capacitively shunted resonant level junction in parallel with an inductor. In the high-transparency regime discussed in 1.7.1, fluxons are predominantly coupled by 4π quantum phase slips. This regime implies that, at the sweet-spot $\phi_{ext} = \pi$, the avoided crossings between (anti-)symmetric superpositions of degenerate fluxons separated by phase 2π should disappear. We calculate how the fluxonium spectrum is affected by the presence of the resonant level using low-energy WKB for arbitrary effective transparency. We also

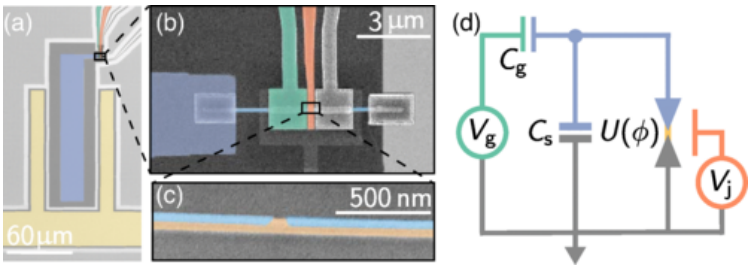

Figure 1.12. A nanowire transmon device where the vanishing charge dispersion was observed [16]. *Reprinted figure with permission from Arno Bargerbos, Willemijn Uilhoorn, Chung-Kai Yang, Peter Krogstrup, Leo P. Kouwenhoven, Gijs de Lange, Bernard van Heck, and Angela Kou Phys. Rev. Lett.* ***124****, 246802 (2020). Copyright 2020 by the American Physical Society.*

show that if the inductive energy of the loop is much smaller than the plasma frequency of the junction, the low-energy Hamiltonian of the circuit is dual to that of a topological superconducting island. These findings can inform experiments on bifluxon qubits as well as the design of novel types of protected qubits.

1.7.3 Chapter 4

In the fourth chapter, we move away from the qubit applications and consider a hybrid planar Josephson junction with an altermagnet (d-wave magnet) inside the normal part. We compute the effect of the altermagnet on the Andreev bound state spectrum in a non-perturbative way, assuming the short junction limit. Unlike in a non-magnetic Josephson junction, the Andreev bound states with opposite spins acquire opposite phase shifts $E(\phi \pm \delta\phi)$, such that the spectrum becomes spin-polarized. When the magnetic order has pure d_{x-y} symmetry with respect to the y direction perpendicular to the junction, the Andreev bound state spectrum acquires a simple form:

$$E = \Delta_0 \sqrt{1 - T(k_y) \sin^2 \frac{1}{2}(\phi \pm \delta\phi(k_y))}, \tag{1.24}$$

where k_y is the transversal momentum (which is a good quantum number here), T is the transparency of the mode with such a transversal momentum and $\delta\phi$ is a phase shift that depends on the length of the junction, altermagnetic coupling, k_y and is opposite for opposite spins. We

also calculate the corresponding total Josephson energy and supercurrent, recovering the possibility of π-junction behaviour, which was predicted earlier [8, 9].

1.7.4 Chapter 5

In this chapter, we investigate the magnetotransport in minimally twisted bilayer graphene. We use a well-established network model [41–43, 48, 49, 81, 82] of chiral ballistic modes (arranged in a triangular network), which applies to samples where the inter-valley scattering can be neglected and an additional perpendicular field is applied. In a certain parametric regime of the phenomenological model (which is expected to hold in the real samples), the 2D transport can be mapped to a 1D random walk. One of the spatial dimensions (along which backscattering of the ballistic modes is not possible) maps to time in the random walk, and the perpedicular magnetic field is mapped onto the electric field. In this way, a mathematical analogue of 1D Bloch oscillations can be observed in the 2D magnetotransport of minimally twisted bilayer graphene, as the oscillations in the magnetoconductace with the magnetic field will have periodicity set by the Bloch frequency.

1.7.5 Chapter 6

The last chapter concerns magnetotransport in 2D materials with open Fermi surfaces, which is a generalization of the model considered in the previous chapter. The stationary Schroedinger equation in the presence of the magnetic field can be mapped to the evolution equation of a particle in a 1D crystal in the presence of an electric field (where time maps to the spatial direction x in which the orbit is open). Due to the Bragg reflection in the 1D crystal as the particle reaches the Brillouin zone boundary, the spatial profile of the corresponding 2D density profile will show periodicity with x. If the wave-function is localized at the lengthscale of the unit cell for a certain x_0, it will be refocused after $\Delta x = (eaB/h)^{-1}$ (a is the lattice constant and B is the magnetic field). Unlike the usual magnetic focusing effect due to the Lorentz force with the focal length $\frac{k_F}{eB}$ (k_F – Fermi momentum), the focusing effect in this chapter is intrinsically quantum.